HAL
open science

Co - Fe - B / Mg O / Ge Spin Photodiode Operating at Telecommunication Wavelength with Zero Applied Magnetic Field

Abdelhak Djeffal, Fabian Cadiz, Mathieu Stoffel, Delphine Lagarde, Xue Gao, Henri Jaffrès, Xavier Devaux, Sylvie Migot, Xavier Marie, Hervé Rinnert, et al.

To cite this version:

Abdelhak Djeffal, Fabian Cadiz, Mathieu Stoffel, Delphine Lagarde, Xue Gao, et al.. Co - Fe - B / Mg O / Ge Spin Photodiode Operating at Telecommunication Wavelength with Zero Applied Magnetic Field. Physical Review Applied, 2018, 10 (4), 10.1103/physrevapplied.10.044049 . hal-02011620

HAL Id: hal-02011620

https://hal.univ-lorraine.fr/hal-02011620v1

Submitted on 8 Feb 2019

HAL is a multi-disciplinary open access archive for the deposit and dissemination of scientific research documents, whether they are published or not. The documents may come from teaching and research institutions in France or abroad, or from public or private research centers.

L'archive ouverte pluridisciplinaire **HAL**, est destinée au dépôt et à la diffusion de documents scientifiques de niveau recherche, publiés ou non, émanant des établissements d'enseignement et de recherche français ou étrangers, des laboratoires publics ou privés.

Co-Fe-B/MgO/Ge Spin Photodiode Operating at Telecommunication Wavelength with Zero Applied Magnetic Field

Abdelhak Djeffal,[1] Fabian Cadiz,[2] Mathieu Stoffel,[1,*] Delphine Lagarde,[2] Xue Gao,[1] Henri Jaffrès,[3] Xavier Devaux,[1] Sylvie Migot,[1] Xavier Marie,[2] Hervé Rinnert,[1] Stéphane Mangin,[1] Jean-Marie George,[3] Pierre Renucci,[2,†] and Yuan Lu[1,‡]

[1] *Université de Lorraine, Institut Jean Lamour, UMR CNRS 7198, campus ARTEM, 2 Allée André Guinier, 54011 Nancy, France*

[2] *Université de Toulouse, INSA-CNRS-UPS, LPCNO, 135 avenue de Rangueil, 31077 Toulouse, France*

[3] *Unité Mixte de Physique, CNRS, Thales, Univ. Paris-Sud, Université Paris-Saclay, 91767 Palaiseau, France*

(Received 24 April 2018; revised manuscript received 2 August 2018; published 19 October 2018)

We report on the growth and study of Co-Fe-B/MgO/Ge(001) spin photodiode by using a combination of both molecular beam epitaxy (MBE) and sputtering methods. An epitaxial growth of MgO on Ge in MBE is achieved by the deposition of MgO at room temperature (RT) followed by a post-growth annealing at 300 °C. The spin detector, which consists of 1.1-nm ultrathin Co-Fe-B layer capped with 5-nm Ta is subsequently grown by sputtering at RT. After a post-growth annealing of the whole structure at 250 °C, we obtain clear evidence of a strong perpendicular magnetic anisotropy in the temperature range 10-300 K. Co-Fe-B/MgO/Ge(001) heterojunctions are then processed into spin photodiodes demonstrating at zero magnetic field a photocurrent helicity asymmetry of about 0.9% at 9 K and 0.1% at RT at the telecommunication wavelength of 1310 nm. The demonstration of a spin photodiode working at a telecommunication wavelength with zero applied magnetic field is of great interest for future applications of the optical transport of spin information.

DOI: 10.1103/PhysRevApplied.10.044049

I. INTRODUCTION

The evolution of microelectronics is guided by Moore's law, which will soon be confronted with fundamental physical limits, thus hampering future developments. For this reason, alternative device concepts exploring new functionalities have been envisioned. Among these, devices that exploit the spin as a new degree of freedom instead of, or in addition to the electron charge, could lead to great benefits. This has led to the birth of a new and very rapidly growing research field called spin-electronics or spintronics [1]. When spintronics is associated with semiconductors, hybrid devices which integrate both ferromagnetic materials and semiconductor materials onto the same chip can be envisioned. This will be of particular interest since all operations such as storing and processing of information could then be integrated within one technology [2]. Remarkable successes have been achieved in this field during the last decade with different semiconductor materials [3–6]. One of the important achievements is the spin injection from a ferromagnetic contact into a semiconductor overcoming the resistance mismatch by inserting a thin oxide tunnel barrier at the metal/semiconductor interface [7]. Moreover, the development of spin-polarized light-emitting diodes (spin-LEDs) in which spin-polarized electrons are electrically injected into the active region of a semiconductor where they recombine radiatively with unpolarized holes to emit right- or left-circularly polarized light is of prime importance. It was found that the ferromagnetic spin injector plays a key role in determining the efficiency of the spin injection [8,9]. In most cases, the spin-LED was studied in III-V-based semiconductors such as GaAs [10–14] or GaN [15–17]. However, the reverse process: a spin photodiode [18], i.e., the electrical detection of a spin-polarized current when a ferromagnetic/insulator/semiconductor heterojunction is illuminated by a circularly polarized light has gained much less attention. Hirohata *et al.* [19] investigated the spin-dependent electron transport at the interface between NiFe and *n*-doped GaAs(110). They reported a 1% relative variation of the photocurrent at room temperature (RT). Taniyama *et al.* [20] studied spin transport across Fe/GaAs(001) and Fe/AlO_x/GaAs(001) heterojunctions. The photocurrent variation was found to be strongly dependent on the applied magnetic field and reaches a maximum of 1.7% at RT. Hövel *et al.* [21] realized a photodetector using a *p-i-n* diode with a GaAs quantum well in the active region and a Fe/Tb multilayer on top of a MgO

*mathieu.stoffel@univ-lorraine.fr
†renucci@insa-toulouse.fr
‡yuan.lu@univ-lorraine.fr

 © 2018 American Physical Society

layer to ensure filtering of the spin-polarized current at zero external magnetic field. The authors obtained a relatively large photocurrent helicity asymmetry of 3% at RT and in remanence. More recently, in order to avoid the use of an external magnetic field, Roca *et al.* [22] and Zhu *et al.* [23] have reported the possibility to operate under an oblique incident angle using in-plane magnetic injectors on top of the semiconductor part of the device.

While most previous studies of spin photodiodes have mainly focused on the GaAs-based semiconductor material, more recently, germanium (Ge) has also emerged as a promising material for spintronics due to its rather large spin-orbit coupling [24] and long electron-spin lifetimes [25]. Electrical spin injection, transport, and detection has been studied experimentally in bulk Ge [5,26]. Very recently, fully epitaxial Fe/MgO/Ge(001) spin photodiodes were experimentally demonstrated showing a net photocurrent variation of about 5% when being excited at 0.95 eV (i.e., 1300 nm) with a 100% circularly right- and left-polarized light [27,28]. The key advantage here, compared to previous GaAs-based spin photodiodes proof-of-concepts, lies in the wavelength range corresponding to the telecommunication wavelength. In order to fulfill the optical selection rules [29], the magnetization needs to be out-of-plane. For this purpose, Rinaldi *et al.* [28] applied an external magnetic field of up to 1.2 Tesla to drive the magnetization of the 10-nm-thick Fe layer to the out-of-plane configuration. However, this appears to be a strong limitation for future practical device applications. Moreover, the Zeeman effect due to a large magnetic field could also complicate the data analysis [30]. Therefore, a layer structure exhibiting a perpendicular magnetic anisotropy (PMA) would be highly desirable. Furthermore, in order to get a sensitive photodetector and to minimize spurious effects such as the magnetic circular dichroism (MCD) effect, one should also minimize the light absorption in the top magnetic layer of the photodiode. To this aim, a magnetic spin detector with a thickness close to one nanometer would be of great interest. The demonstration of the growth of such an ultrathin magnetic spin detector presenting a PMA on Ge for a zero applied magnetic field spin photodiode is, however, still lacking.

In this paper, we investigate the growth and spin-polarized photocurrent properties of an ultrathin Co-Fe-B/MgO spin detector on Ge(001) substrates. We demonstrate that a careful tuning of the growth parameters and post-growth annealing conditions allows us to obtain a spin detector with strong perpendicular magnetic anisotropy in the range 10–300 K. Finally, encouraging results concerning Co-Fe-B/MgO/Ge(001) spin photodiodes operating at zero magnetic field are obtained: a photocurrent helicity asymmetry of about 0.9% is measured at 9 K and is still detectable (about 0.1%) at RT at the telecommunication wavelength of 1310 nm. The demonstration of a spin photodiode working at a telecommunication wavelength and with a zero applied magnetic field is of great interest for future applications on the optical transport of spin information [31].

II. EXPERIMENTAL DETAILS

Nominally undoped Ge(001) substrates (resistivity $>50\,\Omega\,\mathrm{cm}$) are used in this study. The *ex-situ* cleaning of the Ge(001) substrates is checked by atomic force microscopy (AFM) prior to their transfer into the molecular beam epitaxy (MBE) chamber. After in situ deoxidation, 2 nm of MgO are deposited at RT and subsequently annealed at 300 °C for 1 h. The growth is characterized in situ by reflection high-energy electron diffraction (RHEED). The sample is then transferred without vacuum breaking into the sputtering chamber where 0.5 nm MgO is deposited prior to the growth of a 1.1-nm-thick $Co_{40}Fe_{40}B_{20}$ layer at RT. The heterostructure is finally capped by a 5-nm-thick Ta layer. Ex situ annealing is performed using a rapid thermal annealing (RTA) oven under an argon atmosphere at 250 °C for 3 min [14]. The magnetic properties are measured by superconducting quantum interference device (SQUID) magnetometry as a function of temperature in the range 10–300 K.

High resolution scanning transmission electron microscopy (HR-STEM) is performed to characterize the interfacial structure using a probe-corrected JEOL ARM 200 CF operated at 200 kV. High-angle annular dark-field (HAADF) and bright-field (BF) images are simultaneously recorded. Electron energy loss spectroscopy (EELS) maps are recorded with a Gatan Quantum Imaging filter. In order to be able to correct energy drift and estimate the local thickness, the zero loss and the core loss spectra are simultaneously recorded for a dispersion of 1 eV (Dual EELS method). The pixel size of spectrum images (SI) is typically fixed between 0.1 and 0.15 nm. After energy drift correction, the SI are denoised using a principal component analysis method before quantitative analysis. The SI denoising is performed with the multi-statistical analysis plugins for Digital Micrograph "temDM" [32].

Spin photodiodes based on Co-Fe-B/MgO/Ge(001) heterojunctions are processed using standard UV photolithography and Ar^+ ion milling. First, circular mesas with a diameter of 400 μm are defined [inset of Fig. 4(a)]. Then, a second lithography step is used to define both ring-shaped top contacts and the bottom contacts. 150-nm Au/10-nm Ti are deposited as contact materials. Photocurrent measurements are performed at normal incidence under an optical excitation provided by laser diodes (wavelength 980 nm or 1310 nm). The beam is focused onto the sample with a $f = 20$-mm lens (spot diameter of 2.5 μm). The laser power is about 1 mW. The helicity of the laser is modulated between right (σ^+) and left

(σ^-) circularly polarized light at 50 kHz by a photoelastic modulator (PEM), and the corresponding photocurrent intensities $I^{\sigma+}$ and $I^{\sigma-}$ are transformed into a voltage with a transimpedance amplifier (gain 10^5) and detected with a lock-in amplifier. A magnetic field perpendicular to the photodiode is generated by a coil inserted inside a vibration-free closed-cycle cryostat where the sample is mounted.

III. RESULTS AND DISCUSSION

Prior to the growth, we first investigate the cleaning of the initial Ge(001) surface. Sun *et al.* [33] have suggested a method which combines one or more oxidation cycles in a diluted hydrogen peroxide solution followed by dissolution of the oxide in a HCl solution. Following this method, we obtain a rms surface roughness of about 1.3 nm, which is still a rather large value. Figure 1(a) shows an AFM image obtained after dipping a Ge(001) wafer in a 10% HCl solution for 5 min. The rms surface roughness is shown to decrease to about 0.21 nm, which is typical for a planar Ge(001) surface. This substrate is then immediately transferred into the MBE chamber. After 1-h annealing at 500 °C, the RHEED pattern [Fig. 1(b)] measured along the ⟨110⟩ direction exhibits, in addition to the (−1,0) and (0,1) streaks, the typical half-order (−1/2,0) and (0,1/2) streaks. This indicates that deoxidation has occurred leading to the well-known (2 × 1) reconstruction of the clean Ge(001) surface. We then deposit 2 nm MgO at RT onto the Ge(001)-(2 × 1) surface prior to annealing at 300 °C for 1 h. The RHEED patterns measured after annealing along the Ge ⟨100⟩ and ⟨110⟩ directions are shown in Figs. 1(c) and 1(d), respectively. One can recognize that the patterns consist of streaks indicating that MgO grows epitaxially onto the Ge(001)-(2 × 1) surface. We note that when the growth of MgO is directly performed at 225 °C, streaks are no longer observed (not shown here) indicating that the MgO film is polycrystalline. Interestingly, if one considers the MgO RHEED pattern measured along the Ge⟨100⟩ direction [Fig. 1(c)], one can distinguish two families of streaks pointed at by either green or red arrows. The streaks indicated with green arrows correspond to an epitaxial growth relationship of MgO[110]//Ge[100], i.e., with the MgO unit cell turned by about 45° with respect to the Ge unit cell [Fig. 1(e)]. The streaks indicated with red arrows correspond to an epitaxial growth relationship of MgO[100]//Ge[100], i.e., with cube-on-cube growth of the MgO unit cell on the Ge unit cell [Fig. 1(f)]. Since the streaks pointed at by green arrows are more intense than those pointed at by red arrows, we can thus conclude that MgO[110]//Ge[100] corresponds to the major growth direction. This is also the configuration which minimizes the misfit strain (5.2%) and thus the elastic energy. The minority growth direction MgO[100]//Ge[100] corresponds to the configuration which maximizes the misfit strain (25.6%) and thus the elastic energy. This is consistent with previous observations by Petti *et al.* [34]. In fact, the majority growth direction can be explained by the lattice-matching epitaxy (LME) approach, while the minority growth direction agrees with the prediction of the domain-matching epitaxy (DME) approach [35]. The different growth directions are also determined by the interfacial energies related to chemical interactions [34]. After a 2-nm MgO growth, the sample is transferred to the sputtering chamber without vacuum breaking, where MgO(0.5 nm)/Co-Fe-B(1.1 nm)/Ta(5 nm) is deposited at RT.

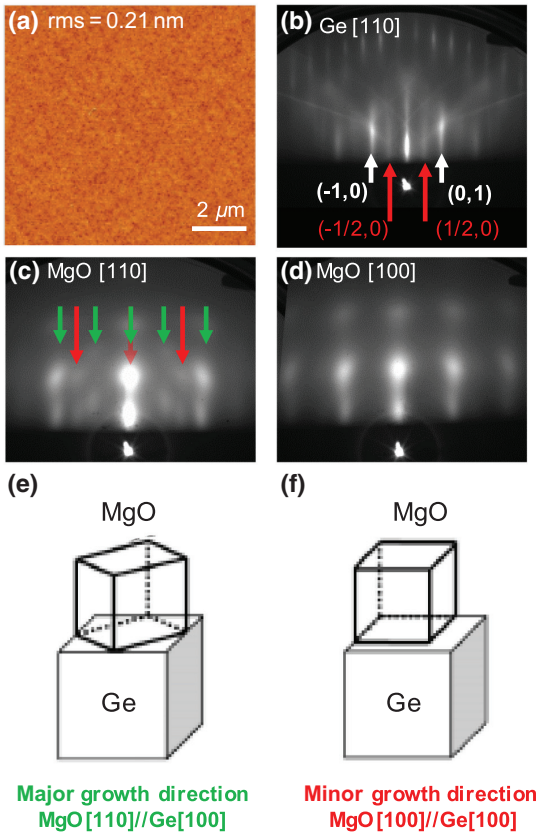

FIG. 1. (a) AFM image obtained for a cleaned Ge(001) substrate before being introduced into the MBE chamber. (b) RHEED pattern on a Ge(001)-(2 × 1) reconstructed surface measured along the [110] direction. RHEED patterns measured after deposition of 2-nm MgO on Ge(001) at RT followed by annealing at 300 °C for 1 h (c) along the Ge [100] direction and (d) along the Ge [110] direction. The green and red arrows in (c) indicate that the growth is textured with two different orientations, either MgO [110]//Ge[100] [green arrows, major growth direction shown in (e)] or MgO[100]//Ge[100] [red arrows, minor growth direction shown in (f)].

We perform STEM EELS combined analyses on the as-grown sample to study the interfacial structure and to get

information on the local chemistry. As shown in Fig. 2(a) recorded with STEM HAADF mode at low magnification, the interfaces between the layers appear very sharp and the layers have constant thickness and low roughness. Because heavy atoms diffuse more electrons than lighter ones, the contrast in STEM HAADF images is linked to the square of the mean atom number. On this micrograph, the Ge substrate is located on the bottom of the image. The MgO layer appears in dark whereas the metal layers appear in white due to Ta. A thin gray layer with contrast close to that of Ge is visible at the interface between MgO and Ta indicating the localization of the Co-Fe-B layer. The granular structure on the top of the multilayer is characteristic of a PtC protective layer deposited during the FIB processing (Pt grains in an amorphous C matrix). Between the metal layers and the PtC capping, a gray layer appears. It indicates that the Ta capping is oxidized at its surface on about 30% of its thickness. The HR-STEM BF images shown in Fig. 2(b) confirm the texture of the MgO layer observed by RHEED during the growth (Fig. 1) with MgO (001)//Ge (001). At the interface between the Ge substrate and the MgO layer [inset of Fig. 2(b)], a phase (2- or 3-atom planes in thickness, pointed at by red arrow) appears with a local lattice constant different from that of MgO or Ge and with a perfect epitaxy on Ge. The nature of this thin layer (less than 0.5-nm thick) will be identified using the spatially resolved EELS mapping. Figure 2(c) shows the element maps extracted from the quantitative analysis of an EELS spectrum image recorded in the area indicated by the red rectangle drawn on the STEM HAADF survey image [inset of Fig. 2(d)]. The Ge substrate is presented on the top of the images. This analysis clearly shows that the interface between Ge and MgO is oxygen-rich. Figure 2(d), constituted with the superposition of Ge_L, Co_L, Mg_K, and Ta_M signals, allows to precisely localize and estimate the thickness of the oxidized Ge layer. The result of the quantitative analysis in this area gives a mean atom ratio of 34% Ge and 64% O, close to GeO_2, without any other element. The thickness deduced from the overall contrast in the oxygen map and from the superposed elemental map is estimated to be about 0.45 nm. This thickness is in total accordance with the 2- or 3-atom planes seen at the interface on BF micrographs [inset of Fig. 2(b)]. This ultrathin GeO_2 layer between Ge and the MgO could be formed during or after the growth of the MgO layer since the RHEED patterns show only a clean Ge surface before MgO growth. Furthermore, the chemical maps allow to confirm the thickness of each deposited layer. MgO and Co-Fe-B layers appear to be 2.3- and 1.3-nm thick, respectively, from the EELS maps. Despite its thin thickness, the Co-Fe-B layer is continuous with a very homogeneous thickness and sharp interfaces on both sides. The ferromagnetic layer is found to have a mean ratio of 55% Fe and 45% Co, which is a bit richer in iron than is expected. It has to be noted that

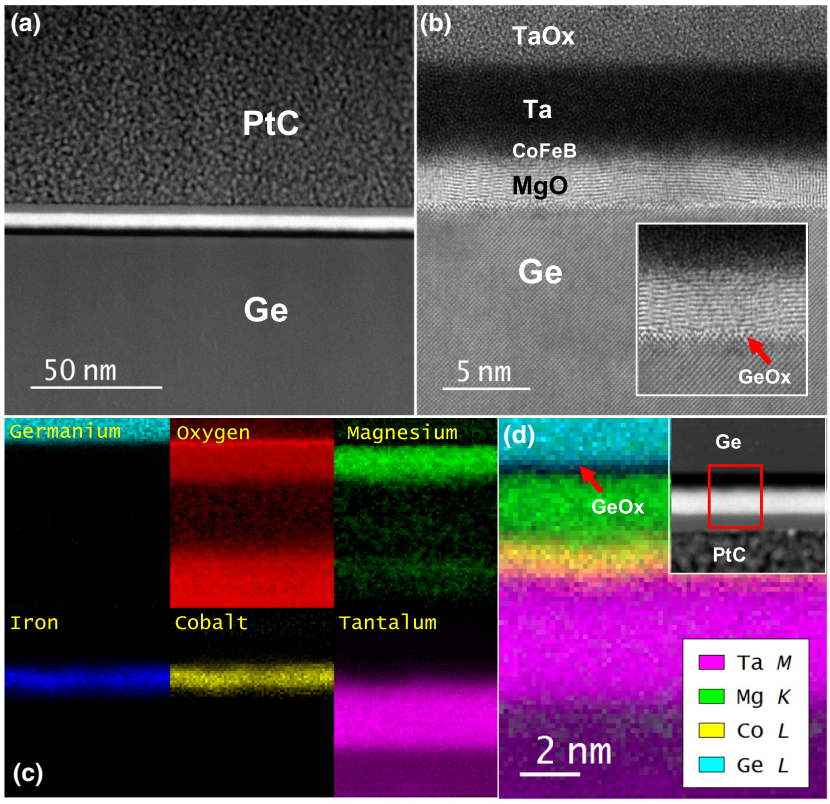

FIG. 2. (a) Low magnification STEM HAADF image of the sample. The MgO layer appears in dark whereas the metal layers appear in white. The gray layer on the top of the multilayer indicates the Ta capping is partially oxidized. The granular structure on the top of the multilayer is characteristic of a PtC protective layer deposited during the FIB processing. (b) HR- STEM BF image showing the good crystallinity of the MgO barrier. The zone axis of the Ge part is [001]. The arrow in the magnified inset points out the crystalline GeO_2 with 2 or 3 monolayers at the Ge/MgO interface. (c) Individual element maps extracted from quantitative analysis of EELS spectrum image (SI). (d) Superposed element map (Ge, Mg, Co, and Ta) precisely showing the distribution of elements at the interface. Inset: HAADF survey image shows where the SI is recorded. The Ge substrate is presented on the top of the images. The contrast Ge signal is not clearly visible at the MgO-Ge interface due to the presence of oxidized Ge. The quantitative analysis yields 34% Ge and 64% O.

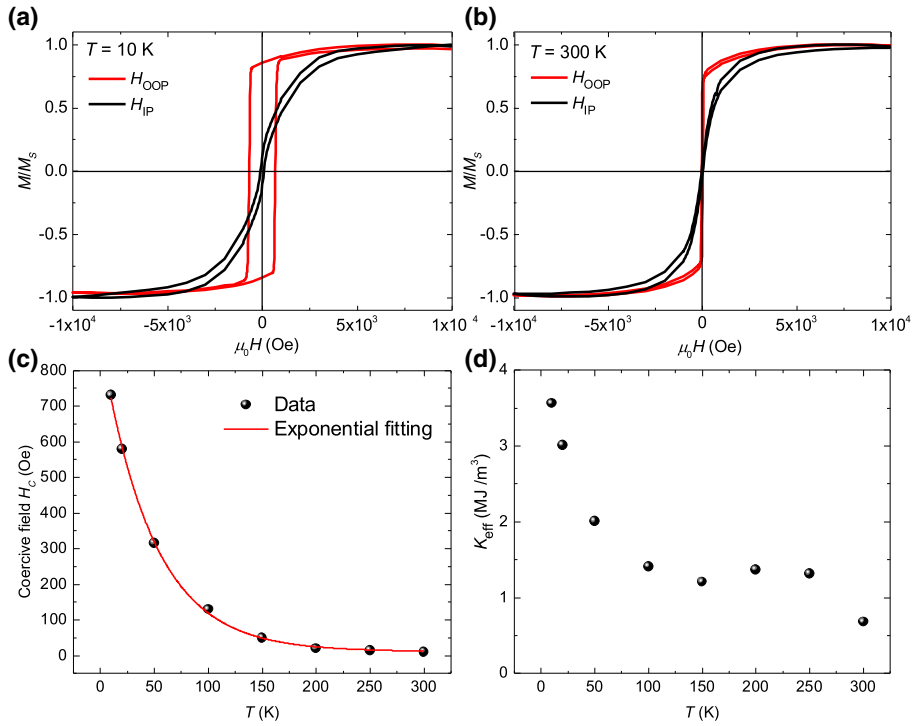

FIG. 3. M-H curves measured with the magnetic field applied either in-plane (H_{IP}, black solid line) or out-of-plane (H_{OOP}, red solid line) at (a) $T = 10$ K and (b) $T = 300$ K. (c) The evolution of the coercive field H_c with temperature. The experimental data are shown as black dots while the fitting using a single exponential decay is shown as a red solid line. (d) Evolution of the effective anisotropy constant with temperature as determined by the area method (see text).

even if boron is detected close to the Co-Fe-B/Ta interface, the signal is too weak for quantitative analysis with the STEM and spectrometer parameters chosen for this EELS mapping. Nevertheless, in our previous work on the EELS mapping of a Ta-capped Co-Fe-B/MgO spin injector deposited on a spin LED, boron diffusion in the Ta layer was detected due to Co-Fe-B crystallization after annealing [36]. As observed from the HAADF images, the Ta capping layer appears oxidized on the top of the surface for 2–3 nm. The atom ratio between Ta and O of 30:70 is very close to that of the stable Ta_2O_5 in the oxidized part. This Ta_2O_5 layer can effectively prevent the penetration of H_2O and oxygen, allowing long aging and high stability of the ultra-thin device.

A post-growth RTA annealing treatment is critical to initialize the crystallization of the Co-Fe-B electrode [37,38] and to establish the perpendicular magnetic anisotropy [14,39]. After RTA annealing at 250 °C for 3 min, the magnetic properties of the Ta/Co-Fe-B/MgO/Ge(001) heterostructure are characterized by SQUID measured at different temperatures. Figure 3(a) shows the magnetization M-H curve measured at 10 K with the magnetic field applied either parallel (H_{IP}, black solid line) or perpendicular (H_{OOP}, red solid line) to the layer structure. One can recognize that the easy magnetization axis is clearly out-of-plane. Moreover, the remnant magnetization reaches approximately 85% of the saturation magnetization. Our measurements thus demonstrate the existence of a PMA for the ultrathin Co-Fe-B/MgO spin detector. It is noteworthy that the PMA can still be observed when the magnetization curves are measured at RT [Fig. 3(b)]. The remnant magnetization still reaches about 73% of the saturation magnetization and the coercive field is about 28 Oe. Figure 3(c) displays the evolution of the coercive field as a function of the temperature. The coercive field clearly decreases as the temperature increases. Our experimental results can be well fitted by a decreasing single exponential function in good agreement with previous results from the literature [40,41]. Finally, we further extract the effective anisotropy constant (K_{eff}) by calculating the difference in area between the magnetization loops measured when the magnetic field is applied perpendicular and parallel to the layers. The results are displayed in Fig. 3(d). Similar to the coercive field, the effective anisotropy constant decreases as the temperature increases. Our results are in good agreement with previous measurements by Yamanouchi *et al.* [42] on Co-Fe-B/MgO films deposited on thermally oxidized Si(001) substrates by rf magnetron sputtering.

The annealed film is then processed to fabricate the device. Figure 4(a) shows a cross-sectional view of the Ge-based spin photodiode. First, we characterize the Schottky barrier height (SBH) at the Co-Fe-B/MgO/Ge contact. Figure 4(b) shows a typical current-voltage characteristic measured from 180 to 300 K without illumination of light, indicating a rectifying Schottky behavior. In this temperature range, the thermionic emission transport mechanism through the Schottky barrier can be mainly considered,

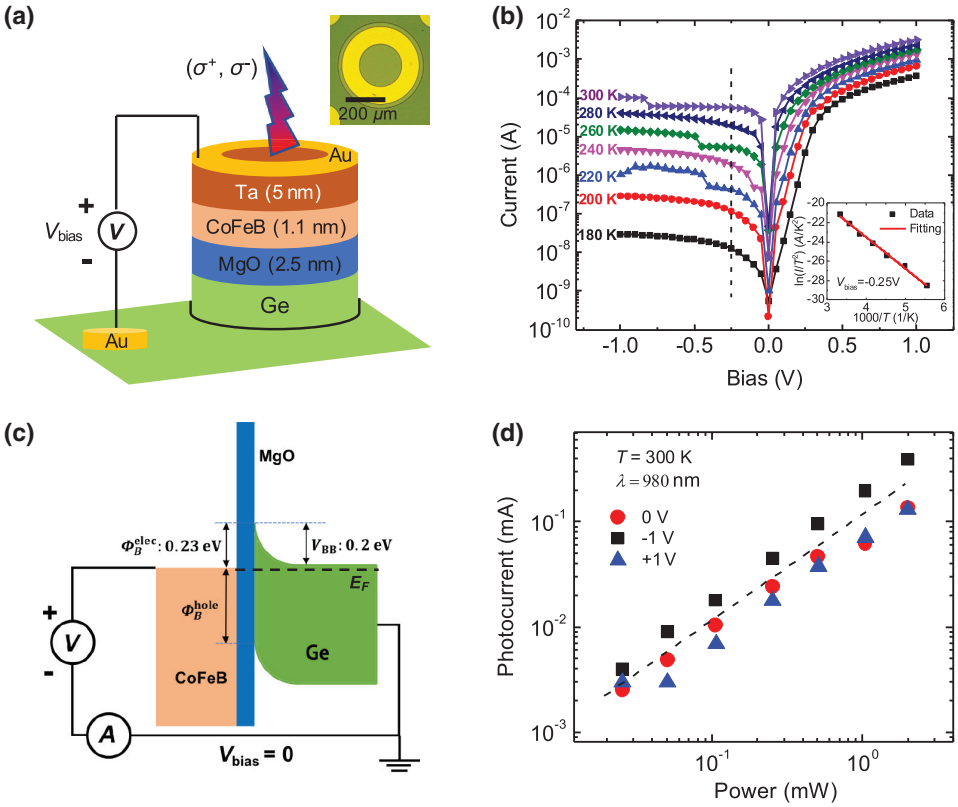

FIG. 4. (a) Schematics of the Ge-based spin photodiode with the top and bottom contacts. Inset: a typical mesa with a diameter of about 400 μm. (b) Current-voltage characteristics measured at different temperatures. Inset: Arrhenius plots $\ln(I/T^2)$ versus $1000/T$ at inversed bias indicated with dashed line in (b). The fitting of slope gives out the Schottky barrier height at an inversed bias condition. (c) Schematic energy band diagram of Co-Fe-B/MgO/Ge contact. (d) RT photocurrent measured as a function of the laser power for different applied biases. The excitation wavelength is fixed at 980 nm.

which can be expressed as [43]

$$I = AA^*T^2\left[\exp\left(\frac{qV}{nk_BT}\right) - 1\right]\exp\left(-\frac{q\phi_B}{k_BT}\right), \quad (1)$$

where A is the contact area, A^* is the Richardson constant, q is the carrier charge, and n is the ideality factor. Since we want to extract the value of SBH for an electron to cross the tunneling barrier, we focus on the part of the negative bias with an inverse condition. When $|V| > 3k_BT/q$, the Eq. (1) can be simplified as

$$I = -AA^*T^2\exp\left(-\frac{q\phi_B}{k_BT}\right). \quad (2)$$

The SBH can be fitted from the slope of the Arrhenius plot [$\ln(I/T^2)$ vs $1000/T$] and we obtain 0.23 eV. This value lies between the value obtained by Jeon *et al.* [43] where the Schottky barrier height was found to be about 140 meV for CoFe/MgO(2 nm)/n-Ge ($n \sim 5 \times 10^{13}$ cm^{-3}) for a MgO thickness of 2 nm, and the one obtained by Zhou *et al.* [44] of about 360 meV for Fe/MgO/n-Ge ($n \sim 5 \times 10^{13}$ cm^{-3}). The Schottky barrier height is dependent on the MgO/Ge interface and thus depends on the growth process. Figure 4(c) shows the schematic energy diagram of the Co-Fe-B/MgO/Ge contact. Figure 5(c) shows the photocurrent as a function of the bias obtained with an excitation wavelength of 980 nm at RT. It is interesting that the photocurrent falls to zero with $V_{\text{bias}} = 0.2$ V, indicating the flat band condition in Ge at this bias voltage. Therefore, we can estimate the built-in band bending V_{BB} in Ge to be about 0.2 eV, as indicated in Fig. 4(c). We also measure the photocurrent as a function of the laser power for different applied bias voltages [$V_{\text{bias}} = -1$ V, 0 V, and $+1$ V, Fig. 4(d)] and for a laser wavelength of 980 nm. The photocurrent exhibits a linear evolution with the laser power for all voltages considered here.

Figure 5(a) shows the evolution of the photocurrent helicity asymmetry, usually defined as $\Delta I/I = (I^{\sigma+} - I^{\sigma-})/[(I^{\sigma+} + I^{\sigma-})/2]$, as a function of the applied magnetic field. $\Delta I/I$ is measured with a laser wavelength λ of 980 nm under $V_{\text{bias}} = -1$ V and $T = 300$ K. It is obvious that $\Delta I/I$ increases with the increase of the magnetic field. For $\mu_0 H = 43$ Oe, $\Delta I/I$ reaches about 0.23%. As the magnetic field is swept from positive to negative values, $\Delta I/I$ changes its signs. Interestingly, at a zero applied magnetic field, the photocurrent helicity asymmetry is not equal to zero and seems to depend on the increasing or decreasing character of the sweep of the magnetic field. We have confirmed this point by performing a sweep in the magnetic field with smaller steps around $\mu_0 H = 0$ as shown in the enlarged view [Fig. 5(b)]. A helicity-dependent asymmetry of the photocurrent is thus evidenced without the need for any external magnetic field, contrary to previous works

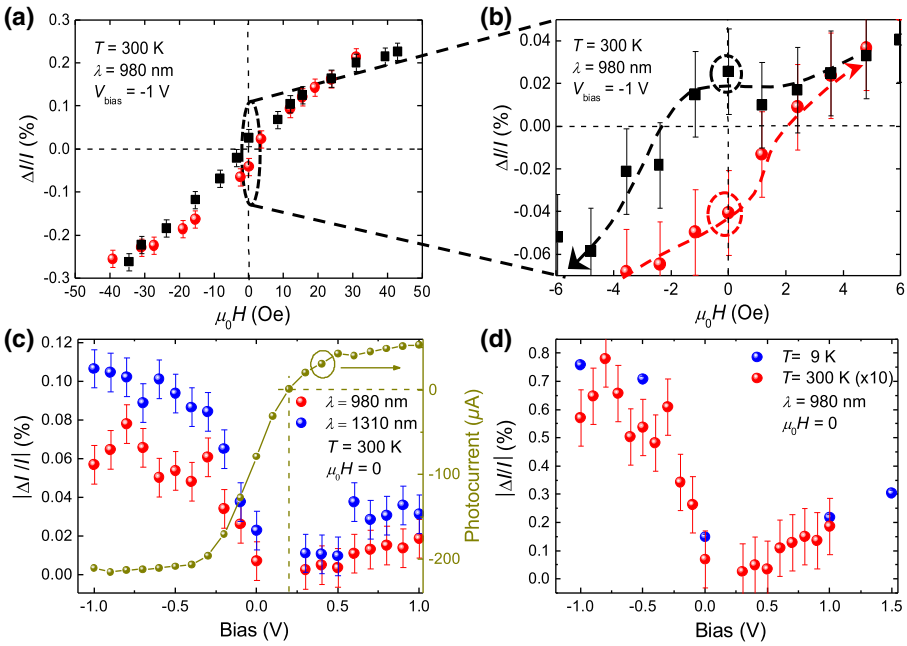

FIG. 5. (a) Evolution of the asymmetry of the helicity-dependent photocurrent $\Delta I/I$ as a function of the applied magnetic field. Red circles and black squares correspond to increasing and decreasing magnetic fields, respectively. (b) Zoom of figure (a) in small magnetic field range. (c) $|\Delta I/I|$ measured as a function of the applied bias for two different excitation wavelengths (980 and 1310 nm) at RT without any applied magnetic field. The bias-dependent photocurrent with 980 nm excitation at RT is also shown. At a bias of 0.2 V (dashed line), the zero photocurrent indicates a flat band condition. (d) $|\Delta I/I|$ as a function of the applied bias measured at 9 and 300 K at zero magnetic field. The excitation wavelength is kept at 980 nm. For comparison with the low temperature measurements, the data measured at RT (shown as red circles) are multiplied by 10.

[28,45]. However, the dependence of $\Delta I/I$ as a function of $\mu_0 H$ does not follow the hysteresis cycle of the Co-Fe-B injector measured by SQUID [Fig. 3(b)]. Since the spin-filtering effect ($\Delta I/I$) of the spin injector could be sensitive to the quality of the Co-Fe-B/MgO interface such as that in a spin-LED system [9], the magnetic field dependence of $\Delta I/I$ can reveal that the Co-Fe-B magnetization can be partially in-plane at the Co-Fe-B/MgO interface, which is very different from the PMA properties of the whole Co-Fe-B layer measured by SQUID [36,46].

Now we focus on the measurement of the photocurrent helicity asymmetry at zero field ($\mu_0 H = 0$). Figure 5(c) shows $|\Delta I/I|$ measured as a function of the applied bias for two different excitation wavelengths (980 and 1310 nm) at RT without any applied magnetic field. The clear variation of $|\Delta I/I|$ as a function of the applied bias is a strong indication that the observed helicity-dependent asymmetry cannot be attributed to the MCD effect [21]. The variation mainly occurs for negative applied biases suggesting that the spin filtering of holes occurs. A similar observation was also reported by Rinaldi *et al.* [28,45] on a device based on an electrode without PMA. Note that for excitation wavelengths $\lambda = 980$ nm and $\lambda = 1310$ nm, electrons and holes do not follow the same dynamics: electrons are photo-generated in the Γ valley and are then very quickly scattered toward the L valley (approximately 200 fs [47]). On the contrary, the holes remain in the Γ valley where they have been photo-generated. Calculations based on density functional theory (DFT) indicate that the asymmetry (between spin up and down carriers) of the tunnel transmission coefficient through the MgO barrier is close to 100% in the Γ valley whereas it is only 35% in the L valley [28]. Thus, holes in the Γ valley will experience a very efficient spin filtering. However, the hole spin relaxation time τ_s is very short, about 100 fs at RT [48]. On the other hand, despite a larger spin relaxation time expected for electrons (0.1–1 ns at RT [49]), the lower $|\Delta I/I|$ could be due to a weaker spin asymmetry of the tunnel transmission coefficient through the MgO barrier in the L valley [28].

In order to estimate the maximum $|\Delta I/I|$ that we could reach, an analytic model has been developed (see Appendix) showing that $|\Delta I/I|_{\max}$ scales with $P_S(1/\lambda_{\text{opt}} + 1/\lambda_R)\lambda_S$ for $\lambda_S \ll \lambda_{\text{opt}}$ or λ_R, where P_S is the photo-generated carrier spin polarization, λ_S is the spin diffusion length, λ_{opt} is the light absorption length, and λ_R is the carrier recombination length. Taking into account a diffusion coefficient D for holes of about 0.0049 $\text{m}^2\ \text{s}^{-1}$ [50] leads

to a hole spin diffusion length $\lambda_S = \sqrt{D\tau_S}$ of about 22 nm. Considering $\lambda_{\text{opt}} \sim 400$ nm at a wavelength of 980 nm [45], an effective lifetime $\tau_R = \lambda_R^2/D$ of about 10 μs [51], and a photo-generated hole spin polarization P_S of about 15% at 980 nm [52], one can expect a maximum of $|\Delta I/I|$ to be about 0.8% at RT. Therefore, the short hole spin relaxation time is a strong limitation that explains the weakness of the detected signal.

Let us now compare the evolution of $|\Delta I/I|$ as a function of the applied bias when the excitation wavelength is changed from 980 to 1310 nm: $|\Delta I/I|$ increases from about 0.06% to about 0.11% at $V_{\text{bias}} = -1$ V. This may be partially due to an increased degree of optical spin orientation P_s at 1310 nm as previously described by Rinaldi *et al.* [45] following the $k{\cdot}p$ calculation by Rioux and Sipe [52] (at this particular wavelength, a polarization of both electrons and holes of about 45% has indeed been predicted, instead of 15% at 980 nm). Moreover, longer spin relaxation times for holes photo-generated at a lower energy are also expected to result in the larger $|\Delta I/I|$ values.

Finally, the temperature dependence of the helicity dependent photocurrent measured for an excitation wavelength of 980 nm is shown in Fig. 5(d). When the temperature decreases from 300 to 9 K, $|\Delta I/I|$ increases from about 0.06% to about 0.8%, i.e., by a factor of approximately 13. This could be linked to the increase of the carrier spin relaxation time (governed by carrier-phonon scattering) at low temperature that was reported for holes between 300 K (approximately 100 fs) [48] and 8 K (approximately 100 ps) [53], and for electrons between 300 K (approximately 1 ns) [54] and 4 K (approximately 100 ns) [25].

Note that the use of an ultrathin Co-Fe-B layer ensures low light absorption in the metallic spin detector layer which is favorable for the realization of a photodetector. We can make a simple estimation of the light absorption with the formula $P(t) = P_0 \exp(-\alpha t)$, where P_0 is the incident intensity and $P(t)$ is the intensity transmitted through a layer of material with thickness t. The attenuation coefficient is α. For a wavelength of 980 nm, the α of Fe is about 4.85×10^5 cm^{-1} [55]. This leads the transmission of our 1.1-nm-thick magnetic electrode to be about 95%. However, it should be noted that for the 40-nm-thick Fe/Tb layer as employed previously in Ref. [21], the transmission is much more attenuated, reaching only about 14%.

IV. CONCLUSIONS

To summarize, we investigate the growth of an ultrathin Co-Fe-B/MgO spin detector on Ge(001) substrates by using a combination of both MBE and sputtering methods. The epitaxial growth of MgO on Ge is observed with two different orientations, i.e., MgO[110](001)//Ge[100](001) corresponding to the major growth direction and MgO[100](001)//Ge[100](001) corresponding to the minor growth direction. The ultrathin Co-Fe-B/MgO spin detector is characterized by a strong perpendicular magnetic anisotropy in the range 10–300 K. The perpendicularly magnetized Co-Fe-B/MgO/Ge spin photodiodes gives rise to a photocurrent helicity asymmetry of about 0.9% at 10 K at 980 nm and of about 0.1% at RT at the telecommunication wavelength of 1310 nm without any applied magnetic field. Additional growth improvements are necessary in order to increase this asymmetry. In particular, the magnetic properties at the Co-Fe-B/MgO interface appear to be deteriorated compared to the magnetic properties of the Co-Fe-B layer itself. Our findings may pave the way for the development of a spin photocurrent detector on Ge(001) substrates for future optical transport of spin information.

ACKNOWLEDGMENTS

We thank Michel Hehn for help to develop the growth of ultrathin Co-Fe-B layer by sputtering. This work is supported by the joint French National Research Agency (ANR)-National Natural Science Foundation of China (NSFC) ENSEMBLE Project (Grants No. ANR-14-0028-01 and No. NNSFC 61411136001), SISTER Project (Grants No. ANR-11-IS10-0001 and No. NNSFC 61161130527) and by the French PIA project "Lorraine Université d'Excellence" (Grant No. ANR-15-IDEX-04-LUE). F.C. and P.R. acknowledge the Grant NEXT No. ANR-10-LABX-0037 in the framework of the Programme des Investissements d'Avenir. X.M. acknowledges Institut Universitaire de France. A.D acknowledges PhD funding from Region Lorraine. Experiments were performed using equipment from the platform TUBE–Davm funded by FEDER (EU), ANR, the Region Lorraine, and Grand Nancy.

APPENDIX I. CALCULATION OF THE MAXIMUM OF PHOTOCURRENT HELICITY ASYMMETRY

We develop a simple analytic model to estimate the maximum of photocurrent helicity asymmetry in our measurement conditions. We have to discriminate between the hole and electron carrier photocurrent generated by optical pumping under the negative bias where the spin photocurrent is maximum. Under these experimental conditions, the external electric field adds up to the built-in Schottky electric field having the effect to drive the electrons out of the tunnel barrier interface region toward the "bulk" Ge and to drive the hole in the ferromagnetic contact through the tunnel barrier. We then mainly observe a hole photocurrent. We demonstrate that the electric field has a dominant effect on the electron photocurrent and mostly no effect on the hole photocurrent. We then determine the equations of holes' transport under pumping and the equations giving the hole photocurrent. Our simplified equations will

slightly depart from the previous coupled electron-hole equations derived by Isella *et al.* [56] by the consideration of specific boundary conditions for a spin-polarized photocurrent due to the presence of a contact resistance played by the tunnel barrier.

1. General transport equations for carriers involving the electric field effect

The general transport equations for pumped carriers' density $n(z)$ under a static electric field, $E(z)$, are

$$\frac{J(z)}{e} = -D\nabla_z n(z) + n(z)e\mu E(z) \text{ and} \tag{A1}$$

$$\frac{dn(z)}{dt} = -\nabla_z J(z) - \frac{n(z)}{\tau_R} + G(z), \tag{A2}$$

where $J(z)$ is the photocurrent, μ is the carrier mobility, $D = kT\tau_p/e$ is the diffusion constant (τ_p is the characteristic collision time), and τ_R represents a certain relaxation time (spin-flip time in the present case). $G(z) = G_0 e^{-\frac{z}{\lambda_{\text{opt}}}}$ is the carrier generation per unit time by optical pumping rate which attenuates with an exponential absorption coefficient (inverse of the absorption length λ_{opt}). The first equation expresses the dual contributions of the respective diffusive term, $-D\nabla_z n(z)$, and the drift term, $n(z)e\mu E(z)$, on the current. The second equation expresses the charge conservation. Depending on the strength of the electric field with respect to a certain critical value, E_c, either the drift or diffusion contribution will be dominant. The development of the coupled equations gives a value of E_c equaling $E_c = D/\mu\lambda_R$ [57] where $\lambda_R (= \sqrt{D\tau_R})$ is the corresponding relaxation length (e.g., the spin diffusion length in the present case).

The examination of the present condition $E \ll D/\mu\lambda_R$ or $E \gg D/\mu\lambda_R$ with $E \cong e\Phi/L_D + E_a$ where Φ is the Schottky barrier height, L_D is its depletion length (of the order of hundreds of 100 nm at low doping case), and E_a is the external electric field applied, leads to the conclusion that the electric field has almost no effect on the hole photocurrent (a very short spin-diffusion length of 22 nm leading to a strong diffusive current). On the contrary, the E field is predominant for the electron photocurrent due to its expected long spin-diffusion length at low doping of the order of 1 μm.

2. Transport equations for holes involving no electric-field effect

We consider now the detailed hole transport equation of density $p(z)$ free of the presence of an electric field. One notes that $p(z)$ is the profile of the optically pumped carrier density, thus the diffusive current J generated in Ge at zero bias can be described by the two equations concerning the spatial distribution and dynamic equilibrium according to

$$\frac{J(z)}{e} = -D\nabla_z p(z) \text{ and} \tag{A3}$$

$$\frac{dp(z)}{dt} = -\nabla_z J(z) - \frac{p(z)}{\tau_R} + G(z). \tag{A4}$$

For spin-polarized carriers, τ_R is the effective carrier recombination time involving the spin-flip term τ_s ($1/\tau_R = 1/\tau_{R0} + 1/\tau_S$) with τ_{R0} being the intrinsic unpolarized hole recombination time.

When $dp(z)/dt = 0$ in the steady-state regime, we get

$$\nabla_z J(z) = -\frac{p(z)}{\tau_R} + G(z)\,. \tag{A5}$$

By injecting equation (A3) into (A5) we obtain

$$D\frac{\partial^2 p(z)}{\partial z^2} = \frac{p(z)}{\tau_R} - G(z)\,. \tag{A6}$$

One notes that $D\tau_R = \lambda_R^2$, where λ_R is the carrier recombination length, and in general $\lambda_R \neq \lambda_{\text{opt}}$.

By resolving the differential equation (A6) we get

$$p(z) = \frac{-G_0/D}{1/\lambda_{\text{opt}}^2 - 1/\lambda_R^2} e^{-(z/\lambda_{\text{opt}})} + \Delta_p e^{-(z/\lambda_R)} \tag{A7}$$

where Δ_p is a constant which can be determined by the boundary condition.

At the interface ferromagnet (FM)/semiconductor (SC) ($z = 0$), we get the current J_s from Eq. (A7):

$$J_s|_{z=0} = -D\nabla_z p(z=0) = -\frac{G_0/\lambda_{\text{opt}}}{1/\lambda_{\text{opt}}^2 - 1/\lambda_R^2} + \frac{\Delta_p D}{\lambda_R} \tag{A8}$$

In fact, J_s can be also expressed as

$$J_s|_{z=0} = -V_s^T p(z=0) = -V_s^T \left(\frac{-(G_0/D)}{1/\lambda_{\text{opt}}^2 - 1/\lambda_R^2} + \Delta_p \right) \tag{A9}$$

where V_s^T is an effective "surface recombination velocity" (related to the tunneling transmission of the barrier).

Therefore, by the combination of Eqs. (A8) and (A9), we can deduce Δ_p as follows:

$$\Delta_p = \frac{G_0}{1/\lambda_{\text{opt}}^2 - 1/\lambda_R^2}\left(\frac{1/\lambda_{\text{opt}} + V_s^T/D}{D/\lambda_R + V_s^T}\right) \tag{A10}$$

The measured photocurrent I_{ph} can be expressed as follows:

$$I_{\text{ph}} = -J_s = V_s^T p(z=0) = V_s^T\left(\frac{-(G_0/D)}{1/\lambda_{\text{opt}}^2 - 1/\lambda_R^2} + \Delta_p\right) \tag{A11}$$

By injecting equation (A10) into (A11), we can get

$$\begin{aligned} I_{\text{ph}} &= \frac{V_s^T}{D}\left[\frac{-G_0}{1/\lambda_{\text{opt}}^2 - 1/\lambda_R^2} + \frac{G_0}{1/\lambda_{\text{opt}}^2 - 1/\lambda_R^2}\frac{(V_s^T + D/\lambda_{\text{opt}})}{(V_s^T + D/\lambda_R)}\right] \\ &= \frac{V_s^T G_0}{(1/\lambda_{\text{opt}} + 1/\lambda_R)}\frac{1}{(V_s^T + D/\lambda_R)} \end{aligned} \tag{A12}$$

For the spin-polarized photocurrent, one can replace $G_0 \to P_S G_0$ (P_S is the spin-polarization of carriers) and $\lambda_R \to \lambda_S$ (λ_S is the spin diffusion length). The spin-polarized photocurrent I_{ph}^S can be expressed as

$$I_{\text{ph}}^S = \frac{P_S V_s^T G_0}{(1/\lambda_{\text{opt}} + 1/\lambda_S)}\frac{1}{(V_s^T + D/\lambda_S)} \tag{A13}$$

The spin-polarization of the photocurrent is determined by the ratio between I_{ph}^S and I_{ph}, and can be expressed as

$$P^{(\text{ph})} = \frac{I_{\text{ph}}^S}{I_{\text{ph}}} = P_S\left(\frac{1/\lambda_{\text{opt}} + 1/\lambda_R}{1/\lambda_{\text{opt}} + 1/\lambda_S}\right)\left(\frac{V_s^T + D/\lambda_R}{V_s^T + D/\lambda_S}\right) \tag{A14}$$

For the measured photocurrent helicity asymmetry in our paper, which can be further examined by the spin-dependent filtering of the FM spin detector as follows:

$$\frac{\Delta I}{I} = P^{(\text{ph})}\left(\frac{V_s^{T\uparrow} - V_s^{T\downarrow}}{V_s^{T\uparrow} + V_s^{T\downarrow}}\right) \tag{A15}$$

where $V_s^{T\uparrow}$ and $V_s^{T\downarrow}$ are surface recombination velocities related to the spin-up and spin-down carriers, respectively. Thus, the maximum of the photocurrent helicity asymmetry can be assumed to be $(\Delta I/I)_{\max} = P^{(\text{ph})}$ when $(V_s^{T\uparrow} - V_s^{T\downarrow})/(V_s^{T\uparrow} + V_s^{T\downarrow}) = 1$.

Generally, $\lambda_S \ll \lambda_R$ or λ_{opt}, so Eq. (A15) can be simplified as

$$\left(\frac{\Delta I}{I}\right)_{\max} = P^{(\text{ph})} = P_S\left(\frac{1}{\lambda_{\text{opt}}} + \frac{1}{\lambda_R}\right)\lambda_S\left(\frac{V_s^T + D/\lambda_R}{V_s^T + D/\lambda_S}\right) \tag{A16}$$

(1) In the limit condition of zero surface recombination velocity ($V_s^T = 0$), most of the photogenerated carriers are blocked by the barrier and recombined in the interface localized states:

$$\left(\frac{\Delta I}{I}\right)_{\max} = P^{(\text{ph})} = P_S\left(\frac{1}{\lambda_{\text{opt}}} + \frac{1}{\lambda_R}\right)\frac{\lambda_S^2}{\lambda_R} \tag{A17}$$

(2) In the limit condition of a large surface velocity (large transmission coefficient), which corresponds to our experimental conditions,

$$\left(\frac{\Delta I}{I}\right)_{\max} = P^{(\text{ph})} = P_S\left(\frac{1}{\lambda_{\text{opt}}} + \frac{1}{\lambda_R}\right)\lambda_S \tag{A18}$$

3. Transport equations for electrons involving the electric field effect

The transport equations in the case of a dominant electric field (case of electrons) are

$$\frac{J(z)}{e} = n(z)e\mu E(z) \text{ and} \tag{A19}$$

$$\frac{dn(z)}{dt} = -\nabla_z J(z) - \frac{n(z)}{\tau_R} + G(z) = 0. \tag{A20}$$

This leads to the resolution of the equation for $n(z)$ of the form

$$n(z) - n(z=0) = \frac{G_0}{\mu E}\frac{1}{1/\lambda_{\text{opt}} - 1/\lambda_E}(e^{-(z/\lambda_{\text{opt}})} - e^{-(z/\lambda_E)}),$$

with $\lambda_E = (eE/m)\tau_p\tau_S$. The boundary condition at the interface with the tunnel barrier leads to $n(z=0) = 0$ in that situation of an opposite current sign between electrons escaping toward the ferromagnetic contact and drift current toward the bulk Ge. The solution of the transport equation then is

$$n(z) = \frac{G_0}{\mu E}\frac{1}{1/\lambda_{\text{opt}} - 1/\lambda_E}(e^{-(z/\lambda_{\text{opt}})} - e^{-(z/\lambda_E)}).$$

[1] S. A. Wolf, D. D. Awschalom, R. A. Buhrman, J. M. Daughton, S. von Molnár, M. L. Roukes, A. Y. Chtchelkanova, and D. M. Treger, Spintronics: A spin-based electronics vision for the future, Science **294**, 1488 (2001).

[2] D. Awshalom and M. E. Flatte, Challenge for semiconductor spintronics, Nat. Phys. **3**, 153 (2007).

[3] R. Jansen, Silicon spintronics, Nat. Mater. **11**, 400 (2012).

[4] Y. Lu, J. Li, and I. Appelbaum, Spin-Polarized Transient Electron Trapping in Phosphorus-Doped Silicon, Phys. Rev. Lett. **106**, 217202 (2011).

[5] Y. Zhou, W. Han, L. T. Chang, F. X. Xiu, M. S. Wang, M. Oehme, I. A. Fischer, J. Schulze, R. K. Kawakami, and K. L. Wang, Electrical spin injection and transport in germanium, Phys. Rev. B **84**, 125323 (2011).

[6] S. Liang, H. Yang, P. Renucci, B. Tao, P. Laczkowski, S. Mc-Murtry, G. Wang, X. Marie, J.-M. George, S. Petit-Watelot, A. Djeffal, S. Mangin, H. Jaffrès, and Y. Lu, Electrical spin injection and detection in molybdenum disulfide multilayer channel, Nat. Commun. **8**, 14947 (2017).

[7] A. Fert and H. Jaffrès, Conditions for efficient spin injection from a ferromagnetic metal into a semiconductor, Phys. Rev. B **64**, 184420 (2001).

[8] Y. Lu, V. G. Truong, P. Renucci, M. Tran, H. Jaffrès, C. Deranlot, J.-M. George, A. Lemaître, Y. Zheng, D. Demaille, P.-H. Binh, T. Amand, and X. Marie, MgO thickness dependence of spin injection efficiency in spin-light emitting diodes, Appl. Phys. Lett. **93**, 152102 (2008).

[9] P. Barate, S. Liang, T. T. Zhang, J. Frougier, M. Vidal, P. Renucci, X. Devaux, B. Xu, H. Jaffrès, J. M. George, X. Marie, M. Hehn, S. Mangin, Y. Zheng, T. Amand, B. Tao, X. F. Han, Z. Wang, and Y. Lu, Electrical spin injection into InGaAs/GaAs quantum wells: A comparison between MgO tunnel barriers grown by sputtering and molecular beam epitaxy methods, Appl. Phys. Lett. **105**, 012404 (2014).

[10] R. Fiederling, M. Keim, G. Reuscher, W. Ossau, G. Schmidt, A. Waag, and L. W. Molenkamp, Injection and detection of a spin-polarized current in a light-emitting diode, Nature **402**, 787 (1999).

[11] Y. Ohno, D. K. Young, B. Beschoten, F. Matsukura, H. Ohno, and D. D. Awschalom, Electrical spin injection in a ferromagnetic semiconductor heterostructure, Nature **402**, 790 (1999).

[12] V. G. Truong, P.-H. Binh, P. Renucci, M. Tran, Y. Lu, H. Jaffrès, J.-M. George, C. Deranlot, A. Lemaître, T. Amand, and X. Marie, High speed pulsed electrical spin injection in spin-light emitting diode, Appl. Phys. Lett. **94**, 141109 (2009).

[13] P. Barate, S. H. Liang, T. T. Zhang, J. Frougier, B. Xu, P. Schieffer, M. Vidal, H. Jaffrès, B. Lépine, S. Tricot, F. Cadiz, T. Garandel, J. M. George, T. Amand, X. Devaux, M. Hehn, S. Mangin, B. Tao, X. F. Han, Z. G. Wang, X. Marie, Y. Lu, and P. Renucci, Bias Dependence of the Electrical Spin Injection into GaAs from CoFeB/MgO Injectors with Different MgO Growth Processes, Phys. Rev. Appl. **8**, 054027 (2017).

[14] S. H. Liang, T. T. Zhang, P. Barate, J. Frougier, M. Vidal, P. Renucci, B. Xu, H. Jaffrès, J. M. George, X. Devaux, M. Hehn, X. Marie, S. Mangin, H. X. Yang, A. Hallal, M. Chshiev, T. Amand, H. F. Liu, D. P. Liu, X. F. Han, Z. G. Wang, and Y. Lu, Large and robust electrical spin injection into GaAs at zero magnetic field using an ultrathin CoFeB/MgO injector, Phys. Rev. B **90**, 085310 (2014).

[15] J. Y. Chen, C. Y. Ho, M. L. Lu, L. J. Chu, K. C. Chen, S. W. Chu, W. Chen, C. Y. Mou, and Y. F. Chen, Efficient spin-light emitting diodes based on InGaN/GaN quantum disks at room temperature: A new self-polarized paradigm, Nano Lett. **14**, 3130 (2014).

[16] J. Y. Chen, T. M. Wong, C. W. Chang, C. Y. Dong, and Y. F. Chen, Spin-polarized spin-nanolasers, Nat. Nanotechnol. **9**, 845 (2014).

[17] A. Bhattacharya, M. Z. Baten, I. Iorsh, T. Frost, A. Kavokin, and P. Bhattacharya, Room-Temperature Spin Polariton Diode Laser, Phys. Rev. Lett. **119**, 067701 (2017).

[18] https://patents.google.com/patent/WO2011141304A2/ru: Resonant diode having spin polarization for optoelectronic conversion.

[19] A. Hirohata, Y. B. Xu, C. M. Guertler, and J. A. C. Bland, Spin-dependent electron transport at the ferromagnet/semiconductor interface, J. Appl. Phys. **85**, 5804 (1999).

[20] T. Taniyama, G. Wastlbauer, A. Ionescu, M. Tselepi, and J. A. C. Bland, Spin-selective transport through Fe/AlO_x/GaAs (100) interfaces under optical spin orientation, Phys. Rev. B **68**, 134430 (2003).

[21] S. HÓğvel, N. C. Gerhardt, M. R. Hofmann, F. Y. Lo, D. Reuter, A. D. Wieck, E. Schuster, W. Keune, H. Wende, O. Petracic, and K. Westerholt, Electrical detection of photoinduced spins both at room temperature and in remanence, Appl. Phys. Lett. **92**, 242102 (2008).

[22] R. C. Roca, N. Nishizawa, K. Nishibayashi, and H. Munekata, Investigation of helicity-dependent photocurrent at room temperature from a Fe/x-AlOx/p-GaAs Schottky junction with oblique surface illumination, Jpn. J. Appl. Phys. **56**, 04CN05 (2017).

[23] L. Zhu, W. Huang, P. Renucci, X. Marie, Y. Liu, Y. Li, Q. Wu, Y. Zhang, B. Xu, Y. Lu, and Y. Chen, Angular Dependence of the Spin Photocurrent in a CoFeB/MgO/n-i-p GaAs Quantum Well Structure, Phys. Rev. Appl. **8**, 064022 (2017).

[24] I. Zutic, J. Fabian, and S. Das Sarma, Spintronics: fundamentals and applications, Rev. Mod. Phys. **76**, 323 (2004).

[25] A. Giorgioni, E. Vitiello, E. Grilli, M. Guzzi, and F. Pezzoli, Valley-dependent spin polarization and long-lived electron spins in germanium, Appl. Phys. Lett. **105**, 152404 (2014).

[26] F. Rortais, C. Vergnaud, A. Marty, L. Vila, J. P. Attané, J. Widiez, C. Zucchetti, F. Bottegoni, H. Jaffrès, J. M. George, and M. Jamet, Non-local electrical spin injection and detection in germanium at room temperature, Appl. Phys. Lett. **111**, 182401 (2017).

[27] C. Rinaldi, M. Cantoni, D. Petti, and R. Bertacco, Epitaxial Fe/MgO/Ge spin-photodiodes for integrated detection of light helicity at room temperature, J. Appl. Phys. **111**, 07C312 (2012).

[28] C. Rinaldi, M. Cantoni, D. Petti, A. Sottocorno, M. Leone, N. M. Caffrey, S. Sanvito, and R. Bertacco, Ge-based spin-photodiodes for room temperature integrated detection of photo helicity, Adv. Mater. **24**, 3037 (2012).

[29] F. Meier and B. P. Zakharchenya, *Optical Orientation* (North-Holland, Amsterdam, The Netherlands, 1984).

[30] P. Renucci, V. G. Truong, H. Jaffrès, L. Lombez, P. H. Binh, T. Amand, J. M. George, and X. Marie, Spin-polarized electroluminescence and spin-dependent photocurrent in hybrid semiconductor/ferromagnetic heterostructures: an asymmetric problem, Phys. Rev. B **82**, 195317 (2010).

[31] R. Farshchi, M. Ramsteiner, J. Herfort, A. Tahraoui, and H. T. Grahn, Optical communication of spin information between light emitting diodes, Appl. Phys. Lett. **98**, 162508 (2011).
[32] Pavel Potapov, www.temdm.com.
[33] S. Sun, Y. Sun, Z. Liu, D. I. Lee, S. Peterson, and P. Pianetta, Surface termination and roughness of Ge (100) cleaned by HF and HCl solutions, Appl. Phys. Lett. **88**, 021903 (2006).
[34] D. Petti, M. Cantoni, C. Rinaldi, S. Brivio, R. Bertacco, J. Gazquez, and M. Varela, Sharp Fe/MgO/Ge (001) epitaxial heterostructure for tunneling junctions, J. Appl. Phys. **109**, 084909 (2011).
[35] J. Narayan and B. C. Larson, Domain epitaxy: A unified paradigm for thin film growth, J. Appl. Phys. **93**, 278 (2003).
[36] B. Tao, P. Barate, X. Devaux, P. Renucci, J. Frougier, A. Djeffal, S. Liang, B. Xu, M. Hehn, H. Jaffrès, J.-M. George, X. Marie, S. Mangin, X. F. Han, Z. G. Wang, and Y. Lu, Atomic-scale understanding of high thermal stability of the Mo/CoFeB/MgO spin injector for spin-injection in remanence, Nanoscale **10**, 10213 (2018).
[37] Y. Lu, B. Lépine, G. Jézéquel, S. Ababou, M. Anlot, J. Lambert, A. Renard, M. Mullet, C. Deranlot, H. Jaffrès, F. Petroff, and J.-M. George, Depth analysis of boron diffusion in MgO/CoFeB bilayer by x-ray photoelectron spectroscopy, J. Appl. Phys. **108**, 043703 (2010).
[38] Z. Wang, M. Saito, K. P. McKenna, S. Fukami, H. Sato, S. Ikeda, H. Ohno, and Y. Ikuhara, Atomic-scale structure and local chemistry of CoFeB/MgO magnetic tunnel junctions, Nano Lett. **16**, 1530 (2016).
[39] S. Ikeda, K. Miura, H. Yamamoto, K. Mizunuma, H. D. Gan, M. Endo, S. Kanai, J. Hayakawa, F. Matsukura, and H. Ohno, A perpendicular-anisotropy CoFeB/MgO magnetic tunnel junction, Nat. Mater. **9**, 721 (2010).
[40] J. Hauschild, H. Fritzsche, S. Bonn, and Y. Liu, Determination of the temperature dependence of the coercivity in Fe/Cr (110) multilayers, Appl. Phys. A **74**, S1541 (2002).
[41] A. Raghunathan, Y. Melikhov, J. E. Snyder, and D. C. Jile, Theoretical model of temperature dependence of hysteresis based on mean field theory, IEEE Trans. Magn. **46**, 1507 (2010).
[42] M. Yamanouchi, A. Jander, P. Dhagat, S. Ikeda, F. Matsukura, and H. Ohno, Domain structure in CoFeB thin films with perpendicular magnetic anisotropy, IEEE Magn. Lett. **2**, 3000304 (2011).
[43] K.-R. Jeon, B.-C. Min, H.-S. Lee, I.-J. Shin, C.-Y. Park, and S.-C. Shin, Single crystalline CoFe/MgO tunnel contact on nondegenerate Ge with a proper resistance-area product for efficient spin injection and detection, Appl. Phys. Lett. **97**, 022105 (2010).
[44] Y. Zhou, W. Han, Y. Wang, F. Xiu, J. Zou, R. K. Kawakami, and K. L. Wang, Investigating the orgin of Fermi level pinning in Ge Schottky junctions using epitaxially grown ultrathin MgO films, Appl. Phys. Lett. **96**, 102103 (2010).
[45] C. Rinaldi, M. Cantoni, M. Marangoni, C. Manzoni, G. Cerullo, and R. Bertacco, Wide-range optical spin orientation in Ge from near-infrared to visible light, Phys. Rev. B **90**, 161304(R) (2014).
[46] B. S. Tao, P. Barate, J. Frougier, P. Renucci, B. Xu, A. Djeffal, H. Jaffrès, J.-M. George, X. Marie, S. Petit-Watelot, S. Mangin, X. F. Han, Z. G. Wang, and Y. Lu, Electrical spin injection into GaAs based light emitting diodes using perpendicular magnetic tunnel junction-type spin injector, Appl. Phys. Lett. **108**, 152404 (2016).
[47] E. J. Loren, J. Rioux, C. Lange, J. E. Sipe, H. M. van Driel, and A. L. Smirl, Hole spin relaxation and intervalley electron scattering in germanium, Phys. Rev. B **84**, 214307 (2011).
[48] E. J. Loren, B. A. Ruzicka, L. K. Werake, H. Zhao, H. M. Van Driel, and A. L. Smirl, Optical injection and detection of ballistic pure spin currents in Ge, Appl. Phys. Lett. **95**, 092107 (2009).
[49] S. Patibandla, G. M. Atkinson, S. Bandyopadhyay, and G. C. Tepper, Competing D'yakonov-Perel' and Elliott-Yafet spin relaxation in germanium, Physica E **42**, 1721 (2010).
[50] O. A. Golikova, B. Ya Moizhez, and L. S. Stilbans, Hole mobility of germanium as a function of concentration and temperature, Sov. Phys. Solid State **3**, 2259 (1962).
[51] E. Gaubas and J. Vanhellemont, Dependence of carrier lifetime in germanium on resistivity and carrier injection level, Appl. Phys. Lett. **89**, 142106 (2006).
[52] J. Rioux and J. E. Sipe, Optical injection and control in germanium: Thirty-band k · p theory, Phys. Rev. B **81**, 155215 (2010).
[53] C. Hautmann, B. Surrer, and M. Betz, Ultrafast optical orientation and coherent Larmor precession and electron and hole spins in bulk germanium, Phys. Rev. B **83**, 161203(R) (2011).
[54] A. Jain, J.-C. Rojas-Sanchez, M. Cubukcu, J. Peiro, J. C. Le Breton, E. Prestat, C. Vergnaud, L. Louahadj, C. Portemont, C. Ducruet, V. Baltz, A. Barski, P. Bayle-Guillemaud, L. Vila, J.-P. Attané, E. Augendre, G. Desfonds, S. Gambarelli, H. Jaffrès, J.-M. George, and M. Jamet, Crossover from Spin Accumulation into Interface States to Spin Injection in the Germanium Conduction Band, Phys. Rev. Lett. **109**, 106603 (2012).
[55] P. B. Johnson and R. W. Christy, Optical constants of transition metals: Ti, V, Cr, Mn, Fe, Co, Ni and Pd, Phys. Rev. B **9**, 5056 (1974).
[56] G. Isella, F. Bottegoni, A. Ferrari, M. Finazzi, and F. Ciccacci, Photo energy dependence of photo-induced inverse spin-hall effect in Pt/GaAs and Pt/Ge, Appl. Phys. Lett. **106**, 232402 (2015).
[57] Z. G. Yu and M. E. Flatté, Spin diffusion and injection in semiconductor structures: Electric field effects, Phys. Rev. B **66**, 235302 (2002).